

The Shape of Eccentricity: Rapid Classification of Eccentric Binaries with the Wavelet Scattering Transform

Priscilla Canizares*

Department of Applied Mathematics and Theoretical Physics, University of Cambridge

Seppe J. Staelens†

*Department of Applied Mathematics and Theoretical Physics, University of Cambridge and
Leuven Gravity Institute, KU Leuven, Celestijnenlaan 200D box 2415, 3001 Leuven, Belgium*

Isobel Romero-Shaw‡

Gravity Exploration Institute, School of Physics and Astronomy, Cardiff University, Cardiff, CF24 3AA, UK

(Dated: March 2, 2026)

The gravitational-wave (GW) detections reported by the LIGO-Virgo-KAGRA (LVK) collaboration have so far been consistent with quasi-circular compact binary coalescences (CBCs). Nevertheless, a small fraction of binaries driven to merge through dynamical interactions in dense stellar environments or in field triples may retain measurable orbital eccentricity when entering the sensitive frequency band of LVK detectors. Confident measurement of eccentricity in the LVK band would be irrevocable evidence for such dynamically-driven mergers; however, eccentric gravitational waveform models are computationally expensive, and performing production-level inference on *all* detected signals is not an efficient use of resources when eccentric signals are expected to be scarce. An intermediate step between *detection* and *analysis*, in which the signal is assessed for the potential presence of eccentricity, could provide quick recommendations for which signals should undergo production-level eccentric inference. We apply the *wavelet scattering transform* (WST) to a large set of synthetic waveforms in realistic noise, and assess the discriminatory power of the WST using simple linear and shallow neural network classifiers. We find that the WST representation enables effective discrimination between eccentric and quasi-circular binaries and discuss the advantages of the compact representation that the WST enables. We demonstrate that the WST is a powerful multi-scale representation tool for the identification of eccentric CBC signals in GW data, achieving $\sim 64\%$ of detection accuracy at a false alarm rate of 10%, with an AUC of 0.844 and an average precision of 0.876. Finally, we investigate the ability of our classifiers to distinguish eccentricity from spin-induced precession effects, and find that they perform well across a range of spin-precession magnitudes. We conclude that the WST will be a powerful tool to identify the fingerprints of eccentricity in CBC signals.

I. INTRODUCTION

Gravitational wave (GW) detections made by the LIGO-Virgo-KAGRA (LVK) Collaboration are yielding exciting inferences about the production mechanisms of merging compact binaries, thus providing better constraints on their formation channels. The most recent Gravitational Wave Transient Catalog, GWTC-4 [1], contains 158 candidates with false alarm rate (FAR) $< 1 \text{ yr}^{-1}$ [2]; the properties of this population appear consistent with being produced via a variety of formation mechanisms, including isolated field triples [3] and dynamical formation in dense star clusters [e.g., 4, 5]. In

contrast to fully isolated binary evolution—which is expected to produce only quasi-circular mergers in the LVK frequency range [6]—a small fraction of dynamically-formed and tertiary-influenced mergers should retain measurable eccentricity close to merger [e.g., 7, 8].

The LVK pipelines have not fully included eccentricity so far due to historical waveform model development lags. Recently, short-author works have used increasingly efficient new eccentric waveform models to place constraints and, in some cases, measure non-negligible eccentricity in CBC signals [e.g., 9–13]. None of the eccentric candidates are confident detections of eccentricity: their interpretation is clouded by missing merger or spin physics in the waveform models, possible confusion with spin-induced precession [14–17], data quality issues [e.g., 18], or low signal-to-noise ratio (SNR) [e.g., 19]. Nonetheless, with growing evidence for dynamical and/or triple-origin mergers in the data, we could anticipate confident detections of eccentricity in the near future [20]: such formation scenarios have a predicted eccentric merger output of $\sim 10\%$.

There are, however, some hard-to-quantify barriers

* pc464@cam.ac.uk

† ss3033@cam.ac.uk

‡ romero-shawi@cardiff.ac.uk

to these expectations. LVK matched-filter searches are tuned to quasi-circular signals, which significantly reduces their sensitivity to eccentric CBC signals [e.g., 20–22]. While unmodelled searches may capture some additional high-mass eccentric sources, we remain observationally biased against observing inspiral-dominated eccentric signals [22–24]. Until recently, eccentric waveform models were near-prohibitively expensive, requiring novel methods like importance-sampling with likelihood reweighting [25] or machine learning [10] to make their use in analysis feasible. More efficient eccentric waveform models now exist [e.g., 26–29], but they retain the limitations described above, and/or are still much slower than their quasi-circular counterparts. Exacerbating this expense, the LVK’s detection efficiency has increased impressively since O1, and there are now hundreds of new CBC signals per observing run. With eccentric mergers constituting a relatively small fraction of the underlying physical population, and with search methods biased against detecting them, we argue that running eccentric analyses on all LVK candidates may not be well-justified.

It is reasonable, therefore, to propose a computationally efficient filtering step in-between detection and eccentric analysis. Machine learning is optimally-suited to such a problem, being highly successful in areas requiring pattern recognition and prioritising speed. Indeed, [29] designed and trained a two-dimensional convolutional neural network (2D CNN) to study Q-scans of GW data and identify the presence of eccentricity in the signal. Similarly, [30] proposed a transformer-based approach to detect eccentricity from GW scalograms.

Here, we address this problem using a wavelet scattering transform (WST) representation of simulated GW strain data. This approach circumvents the need to process scans or images by operating directly on a compressed representation of the signal. We employ a state-of-the-art eccentric waveform model incorporating higher-order modes [27], and construct efficient, interpretable classifiers for eccentricity detection.

The WST is a signal-processing technique that builds a multi-scale, multi-orientation representation of the data in the form of coefficients that capture key structural features [31, 32]. The WST has already been demonstrated as a powerful tool to classify and characterise glitches in interferometer strain data, leading to improvements in robust signal detection [33]. Outside of GW data analysis, the WST has been used in cosmology, see [34–38], as well as metrology, finance and image analysis, see e.g. [39–43].

In this work, we find that the WST shows promise for extracting the characteristic features of GW signals from eccentric CBCs in realistic noise. We train and test three different classifier architectures: logistic regression, one-dimensional CNN, and two-dimensional CNN. While these methods will likely benefit from future improvements—such as altering our reference frequency-based definition of eccentricity to one that defines eccentricity at a fixed number of cycles before merger—we find that they are already able to correctly distinguish be-

tween eccentric and quasi-circular signals in the majority of the test set, even when the quasi-circular signals contain spin-induced precession.

This paper is organized as follows. In Sec. II, we introduce the dataset we use in this study and the wavelet scattering transform. We also describe the classifiers considered in this work, namely logistic regression, a one-dimensional convolutional neural network (1D-CNN), and a two-dimensional convolutional neural network (2D-CNN), and present their benchmarking. In Sec. III, we present the results. We finish in Sec. IV by discussing the implications of our findings and outline conclusions and future directions.

II. METHODS

A. Waveform Generation: SEOBNRv5EHM

Using Bilby [44, 45], we generate synthetic strain data comprising simulated waveforms injected into detector noise. We initialise the detectors with realistic noise, i.e., using Gaussian noise coloured by O4 noise curves ("realistic noise" hereafter).

Eccentric waveforms are produced using the SEOBNRv5EHM approximant [46], an effective-one-body, multipolar waveform model describing eccentric binary black hole (BBH) systems with component spins aligned with or against the orbital angular momentum. Priors on the intrinsic parameters are defined within Bilby. The dimensionless component spin magnitudes are drawn from aligned-spin priors spanning nearly the full physical range, $a \in [0, 0.99]$, and the relativistic anomaly is sampled uniformly in $[0, 2\pi]$. Component masses $m_{1,2}$ are uniformly sampled in $[10, 40] M_\odot$, while the luminosity distance is sampled through the default Bilby-prior in the range $[100, 800]$ Mpc—ensuring a distribution that is uniform in comoving volume and source frame time.

The eccentricity at a reference frequency of 10 Hz, e_{10} , is sampled uniformly within each class: the classification task is to distinguish eccentric systems ($e_{10} \in [0.01, 0.5]$) from non-eccentric systems ($e_{10} \in [0.001, 0.01]$). While a log-uniform prior is commonly adopted in GW data analysis, uniform sampling ensures balanced class populations during training. The threshold value $e_{10}^{\text{thr}} = 0.01$ adopted here is a practical choice. Alternative definitions of eccentricity that do not rely on a reference frequency are also possible [14, 47, 48].

Waveforms are generated in the frequency domain over the range 10 Hz–1024 Hz, where the upper cutoff corresponds to half the sampling rate f_s . Each signal has a duration of 128 s and is transformed to the time domain via an inverse Fast Fourier Transform (FFT). The geocentric merger time is sampled uniformly from 126 ± 0.1 s, and all waveforms are aligned at merger time. Unless otherwise stated, all six multipoles [49] available in SEOBNRv5EHM are included.

The simulated signals are injected into noise realizations of the two Advanced LIGO detectors and the Advanced Virgo detector. An 8s window around the estimated peak at merger, t_m , is extracted, defined as $[t_m - 7.8\text{s}, t_m + 0.2\text{s}]$. The resulting strain data segments are whitened, and the network signal-to-noise ratio (NSNR) is computed across the detector network. Samples with NSNR < 15 are discarded to ensure confident detectability while preserving realistic detector noise conditions for training and evaluation.

For this study, we generate approximately 120,000 waveforms and compute their corresponding WST representations. The resulting dataset consists, for each signal and detector, of the scattering coefficients C and the associated time bins T_b , where $T_b \ll T \cdot f_s$ and $T = 8\text{s}$ is the total duration of the signal segment considered.

B. Wavelet Scattering Transform

The wavelet scattering transform (WST) is a hierarchical filtering framework that combines wavelet convolutions with modulus and averaging operations to produce a multiscale representation of a signal. The resulting set of scattering coefficients is stable to small deformations and preserves higher order statistical structure, enabling an informative yet compressed characterization of the data [50]. The WST coefficients encode localised structure and cross-scale dependencies, providing sensitivity to morphological waveform features such as those induced by orbital eccentricity [31, 32, 39].

In what follows, we present the formulation of the one-dimensional WST. In practice, we implement the transform using the `Kymatio` package [51], which computes the required convolutions efficiently in the Fourier domain using FFT.

The WST is, in general, parameterised by two quantities, J and Q , see App. A. Given a sampling frequency f_s , the parameter J determines the maximum averaging scale:

$$\tau_J = \frac{2^J}{f_s}, \quad (1)$$

that is, the largest temporal scale over which the scattering coefficients are averaged. Increasing J , therefore, increases translation invariance while reducing temporal resolution. On the other hand, Q specifies the number of wavelets per octave (see App. A), and thus determines the sampling density along the frequency axis. Larger values of Q increase the frequency resolution by providing a finer discretisation of scales.

The WST is constructed using complex Morlet wavelets $\psi_{j,q}(t)$, which are localised in both time and frequency. The wavelets are indexed by discrete scale and frequency indices (j, q) , where $j \in \{0, \dots, J-1\}$ labels the dyadic scale 2^j , and $q \in \{1, \dots, Q\}$ indexes the

wavelets within each octave:

$$\psi_{j,q}(t) = \frac{e^{i(2\pi f_{j,q} t)}}{\sigma(f_{j,q}, Q)\sqrt{2\pi}} e^{-\left(t^2/(2\sigma(f_{j,q}, Q)^2)\right)}, \quad (2)$$

where $f_{j,q}$ and $\sigma(f_{j,q}, Q)$ are the centre frequency and width parameter respectively (see App. A).

The scattering coefficients are computed hierarchically. The zeroth-order coefficient, S_0 , is a local averaged representation of the signal defined as:

$$S_0(t) = (h * \phi_J)(t) \quad (3)$$

where: $(h * \phi_J)(t) = \int h(\tau)\phi_J(t - \tau)d\tau$, and ϕ_J is a low-pass filter with effective width τ_J .

The first-order scattering coefficients, S_1 , are obtained by convolving the signal with a wavelet, applying the modulus, and low-pass averaging:

$$S_1(t, j_1, q_1) = \left(|h * \psi_{j_1, q_1}| * \phi_J \right)(t). \quad (4)$$

These coefficients measure the averaged amplitude of signal fluctuations localized near the scale-frequency index (j_1, q_1) while suppressing high-frequency temporal variations.

Second-order scattering coefficients, S_2 , are computed recursively by applying a second wavelet transform to the first-order coefficients, Eq. 4:

$$S_2(t, j_1, q_1, j_2, q_2) = \left(\left| |h * \psi_{j_1, q_1}| * \psi_{j_2, q_2} \right| * \phi_J \right)(t), \quad (5)$$

with the constraint $j_2 > j_1$, to ensure that the second order wavelet probes amplitude modulations occurring at longer timescales than those captured by the first wavelet. Hence, S_2 coefficients recover information lost during the first averaging step and encode correlations between structures at different scales. Averaging with ϕ_J ensures that all scattering coefficients are invariant to translations up to a scale τ_J .

In a similar way, higher-order coefficients can be defined recursively. However, their amplitudes decrease rapidly with order, and most of the relevant information is captured by the first two orders [31]. Accordingly, in this work we restrict our analysis to orders ≤ 2 and consider the set of scattering coefficients

$$S \equiv \{S_0, S_1, S_2\}. \quad (6)$$

It follows that the WST representation of the GW strain signal provides a multiscale, deformation-stable representation that captures higher-order structure and amplitude modulations, including those induced by orbital eccentricity. Illustrative examples are shown in Fig. 1.

C. WST-Based Classifiers for Eccentricity Detection

CBCs with non-zero orbital eccentricity produce GW signals whose time-frequency structure differs from quasi-

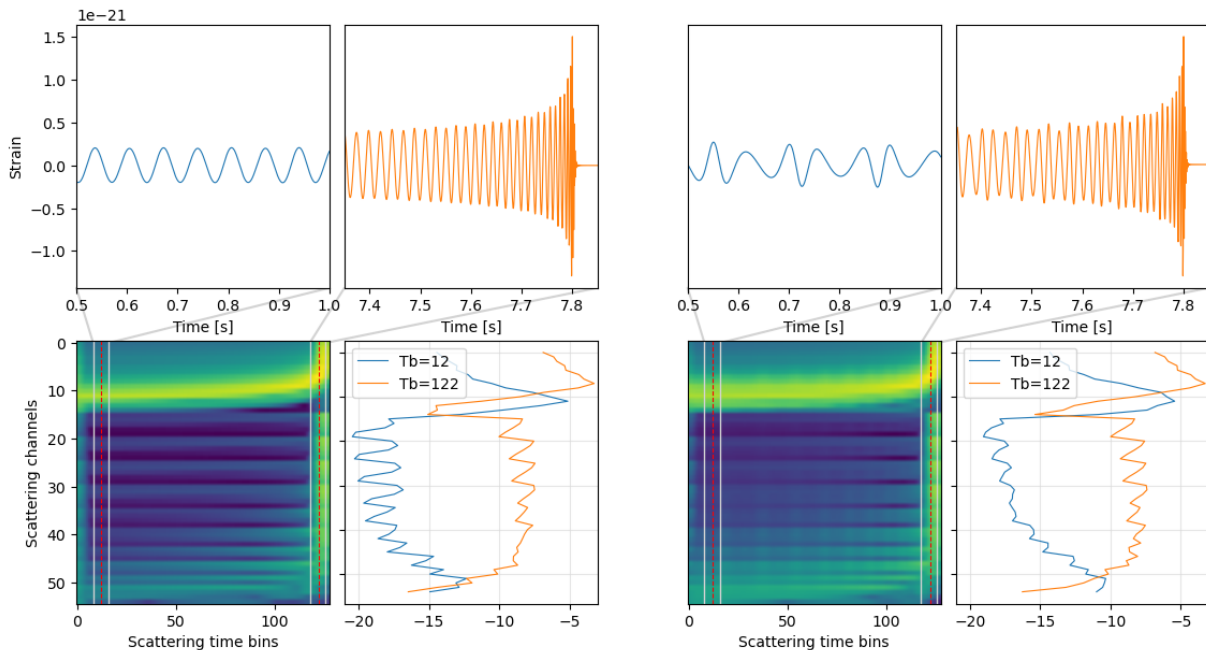


FIG. 1. Illustrative example of a (*left 4 panels*) quasi-circular and (*right 4 panels*) eccentric ($e = 0.3$ at 10 Hz) waveform, and their corresponding $(J, Q) = (7, 2)$ WST coefficients (on a logarithmic scale). The binary masses are 12 and 18 M_{\odot} , at a luminosity distance of 100 Mpc. The top row shows two 0.5 s windows of the waveform, where the first represents the inspiral and the second the merger. The bottom row represents all WST coefficients in the left panel, as well as a slice at two time bins T_b in the right panel, corresponding to the different phases in the top row. From these plots, it is clear that, as expected, the WST coefficients representing the eccentric binary distribute the power across the channels more evenly. It should be noted that the top 15 channels in the bottom row represent first-order scattering coefficients, and the rest second-order.

circular inspirals [47, 52, 53]. Eccentric systems radiate power into multiple harmonics of the orbital frequency, yielding broader and more structured time-frequency energy distributions. Fig. 1 exemplifies this by visualising the WST coefficients of a circular and an eccentric system.

In this section, we describe how the WST is used to extract features associated with orbital eccentricity, which serve as inputs to classifiers designed to evaluate its effectiveness in identifying eccentric systems. Specifically, we consider three data-driven approaches: (a) logistic regression, (b) a one-dimensional convolutional neural network (1D-CNN), and (c) a two-dimensional CNN (2D-CNN).

To quantify the information encoded in the WST, we define energy-based features and compute first-moment statistics from the scattering coefficients to characterise their energy distribution. This separation allows us to distinguish *shape* information, reflecting the relative distribution of power across scales, from *scale* information, reflecting the overall amplitude.

Hence, for each event n , detector d , and scattering scale (channel) c , we define the scale-resolved energy:

$$E_{n,d,c} \doteq \sum_t S_{n,d,c,t}^2 \quad (7)$$

where $S \in \mathbb{R}^{N \times D \times C \times T_b}$ is the WST of the data (6), N

and D the total number of waveforms and number of detectors respectively; and C and T_b denote the number of frequency coefficients (scattering sub-bands) and time bins. In addition to Eq. (7), we define the following energy-based feature representation:

i) Shape features— To isolate shape/morphology information, we define the normalized relative energy:

$$R_{n,d,c} = \frac{E_{n,d,c}}{E_{n,\text{tot}}} \in \mathbb{R}^{DC}, \quad (8)$$

where $E_{n,\text{tot}}$ is the sum over the WST coefficients. Because both numerator and denominator scale quadratically with the strain amplitude, this representation is approximately invariant under overall amplitude rescaling and, thus, to the SNR. We take the logarithm of these data values, to bring all the coefficient values to the same order of magnitude and prevent smaller coefficients from being damped out. Thus, we construct the following feature vector for each event n :

$$\mathbf{x}_n^{(\text{shape})} = \text{vec}[\log(R_{n,d,c})] \in \mathbb{R}^{DC}. \quad (9)$$

ii) Scale features— To reintroduce amplitude information, we introduce shape features with an additional scalar *scale* parameter

$$s_n = \log(1 + E_{n,\text{tot}}), \quad (10)$$

TABLE I. Performance of the logistic regression classifier in terms of the area under the (ROC-)curve, AUC, and true-positive rate, at fixed false-alarm rate, TPR_{FAR} , when applied on the test set. The numbers between brackets denote the relative gains with respect to the "shape only" features.

Features	AUC	$\text{TPR}_{0.1}$	$\text{TPR}_{0.01}$	$\text{TPR}_{0.001}$
Shape (i)	0.798	0.534	0.372	0.311
Scale (ii) + (i)	0.799	0.536 (+0.3)	0.373 (+0.1)	0.316 (+1.6)
Moments (iii)	0.815	0.554 (+3.7)	0.379 (+1.7)	0.281 (-9.6)
All	0.819	0.568 (+6.5)	0.399 (+7.1)	0.333 (+6.9)

which summarizes the total energy of the scattering representation across all detectors and wavelet scales. Since the scattering coefficients scale linearly with the strain amplitude, $E_{n,\text{tot}}$ scales quadratically with the overall strain amplitude, see Eq. (4) and (5). Consequently, s_n correlates with waveform parameters that control the signal strength, such as the source distance, component masses and inclination.

iii) Features based on detector statistics— To capture correlations across detectors, and reduce noise effects, we compute for each frequency scale, c , the mean and variance of $E_{n,d,c}$ across detectors. We also compute the mean, variance, skewness, and kurtosis of the scattering coefficients S over time, and subsequently average these quantities across detectors. These features are constructed to encode both the scale-dependent energy content and the variability between detectors.

1. Logistic Regression

To determine whether the WST coefficients encode eccentricity primarily through their scale, shape, moments, or a combination of these properties, we apply a logistic regression (LR) classifier to the data. This allows us to directly assess the discriminative power of each feature representation. The shape (Eq. 9) and scale (Eq. 10) features can be combined into a single feature map, defined as

$$\mathbf{x}_n^{(\text{shape+scale})} = [\log(R_{n,d,c}), s_n] \in \mathbb{R}^{D \cdot C + 1}. \quad (11)$$

This combined representation captures variations associated with signal strength, such as source distance and orientation, together with shape features encoding eccentricity information.

Training, threshold calibration, and evaluation— A single stratified split of the dataset into training, validation, and test subsets is used for all models. This ensures that differences in performance arise solely from the feature representations. The regularization parameter is selected via cross-validation (CV) on the training and validation sets using the area under the receiver operating characteristic curve (AUC).

Following training, the decision threshold is calibrated on the validation set using only "negative" (non-eccentric) samples, targeting fixed false alarm rates

(FARs) of (0.1, 0.01, 0.001). The resulting thresholds are then held fixed and applied to the test set.

Table I shows the AUC and the true positive rate (TPR) at fixed FAR, summarizing the performance of the LR classifier. The classifier achieves AUC values $\gtrsim 0.8$ across feature configurations, indicating that the WST-derived features contain significant eccentricity information to distinguish between eccentric and non-eccentric classes.

Using shape features alone provides a strong baseline (AUC = 0.798), while adding scale information yields only marginal gains across all operating points. In contrast, incorporating moments improves both AUC and TPR at intermediate FAR, though performance decreases at the lowest FAR when moments are used alone. The full model combining all feature groups achieves the best performance at all FARs, reaching a relative TPR improvement of $\sim 7\%$ across target FARs compared to shape-only features. These results indicate that shape features capture most of the eccentricity information, while moments and scale provide complementary contributions that improve performance.

2. One-Dimensional CNN

We have seen (Sec. II C 1) that the WST coefficients carry sufficient information to detect eccentricity with a linear classifier such as LR, achieving AUC ~ 0.8 and TPR ~ 0.55 at FAR = 0.1%.

To assess whether a nonlinear classifier can further improve the detection efficiency of the WST, while exploiting the temporal structure of the scattering coefficients, we design a one-dimensional convolutional neural network (1D-CNN).

Each detector in the network has distinct characteristics, most notably different noise power spectral densities and antenna response patterns. To account for these differences while learning common signal features, we construct a 1D-CNN architecture, shown in Fig. 2, that takes as input the WST representation of the data from each detector. The network applies a shared convolutional block to the WST of each detector, encouraging the extraction of features that are consistent across the detector network. The resulting embeddings are subsequently fused to form a joint representation that captures the coherent signal features present in the data.

Therefore, the input is a WST tensor of the form: $\mathbf{X}_n \in \mathbb{R}^{B \times D \times C \times T_b}$, where B is the batch size, D the number of detectors, C the number of WST frequency channels, and T_b the number of time bins. For each detector d , the slice $\mathbf{X}_{n,d} \in \mathbb{R}^{B \times C \times T_b}$ is processed independently by a shared convolutional block, ensuring that the learned filters capture detector-independent temporal signatures.

The synthetic data are aligned at merger to make the time axis consistent across events on the same detector. This alignment ensures that corresponding temporal fea-

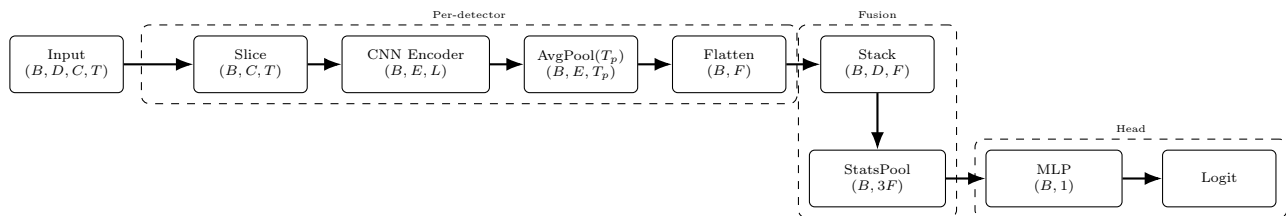


FIG. 2. Block diagram of the 1D-CNN designed for eccentricity detection. Data from different detectors are encoded separately by a shared Conv1d with three convolutional blocks and intermediate max-pooling for temporal downsampling. Feature maps are averaged into T_p bins, producing fixed-length detector embeddings. These are fused (joined) using first order statistics, and the resulting representation is classified by a shallow MLP to yield the final probability value.

tures occur at the same relative positions in the scattering representation and is key for extracting meaningful temporal features across the detector dataset, allowing the network to learn consistent temporal patterns associated with eccentricity. Although times of arrival are slightly offset between detectors for the same event, as is the case for real detections, this effect is mitigated by the modulus operation of the WST and the fact that patterns for each detector are extracted independently, Fig. 2.

The 1D-CNN encodes the WST data into a lower-dimensional representation for each event and detector across channels and time bins. The encoder consists of three convolutional blocks, each composed of a 1D convolutional layer followed by batch normalisation and a ReLU activation function, with max-pooling applied after the first two blocks to reduce the temporal dimension. This structure progressively reduces the number of feature channels from $C \rightarrow 64 \rightarrow 32 \rightarrow 16$, using kernel sizes $(7, 5, 3)$. The resulting embedding is given by

$$\mathbf{H}_{n,d} \doteq f_{\text{cnn}}(\mathbf{X}_{n,d}) \in \mathbb{R}^{E \times L}, \quad (12)$$

where $E = 16$ is the number of embedding channels and $L = \text{floor}(T_b/2)$ denotes the reduced temporal dimension. This representation captures learned temporal correlations across WST channels at multiple time scales.

To obtain a fixed-length, merger-aligned summary, we apply adaptive average pooling to T_p time bins,

$$\tilde{\mathbf{H}}_{n,d} = \text{Pool}_{T_p}(\mathbf{H}_{n,d}) \in \mathbb{R}^{E \times T_p}. \quad (13)$$

In this way, the time axis is divided into T_p coarse temporal segments, producing a compact representation of the scattering coefficients. The pooled representation is then flattened to obtain the final detector embedding

$$\mathbf{e}_{n,d} = \text{vec}(\tilde{\mathbf{H}}_{n,d}) \in \mathbb{R}^{E \cdot T_p}. \quad (14)$$

To construct a joint detector representation, we pool across the detector dimension using three summary statistics, which were found to provide the best performance in the LR analysis (Sec. II C 1): the mean, maximum, and summed squared amplitude (energy). These statistics capture complementary aspects of the detector responses, including coherent signal strength and

detector-dependent variability arising from antenna response and noise realisations. The detector embeddings are stacked into a detector-set representation

$$\mathbf{Z}_n = [\mathbf{e}_{n,1}, \dots, \mathbf{e}_{n,D}] \in \mathbb{R}^{D \times (E \cdot T_p)}, \quad (15)$$

where $\mathbf{e}_{n,d}$ denotes the embedding of detector d for event n —the pooled statistics form the final feature vector, $\mathbf{p}_n \in \mathbb{R}^{3(E \cdot T_p)}$, which is then passed to a two-layer multilayer perceptron with ReLU activation and dropout of 0.3. The network outputs a scalar logit, which defines the eccentric versus non-eccentric classification decision. With default parameters— $T_p = 6$, an intermediate MLP layer of size 128, and $(J, Q) = (7, 2)$ —the model has 74 321 trainable parameters.

3. Two-Dimensional CNN

As a final experiment, we replace the 1D-CNN with a two-dimensional CNN. The input consists of the logarithmically rescaled [54] WST coefficient tensors, with convolutional kernels operating along both the temporal (T_b) and channel (C) dimensions. The three detectors are treated as separate input channels, analogous to the RGB channels in image analysis. This formulation enables direct comparison with image-based CNN approaches, where the input is typically a time–frequency representation such as a spectrogram.

The network architecture is designed to resemble the `ecc_sepconv` model of Ref. [29], and is implemented in PyTorch [55]. The core of the model consists of separable convolutional layers followed by fully connected layers. A schematic overview is shown in Fig. 10. The number of channels in successive convolutional blocks increases as $32 \rightarrow 64 \rightarrow 128 \rightarrow 128 \rightarrow 256$, while the kernel sizes decrease as $5 \rightarrow 5 \rightarrow 5 \rightarrow 3 \rightarrow 3$. A dropout rate of 0.2 is used to mitigate overfitting. The fully connected layers reduce the feature dimension as $64 \rightarrow 32 \rightarrow 16$, followed by a single output node. With these settings, the model contains 86 369 trainable parameters.

TABLE II. Comparison of detection performance for WST data computed on the same dataset, but with $Q = 1, 2$ and fixed $J = 7$. Shown are the mean and standard deviation across $K = 10$ folds. Results are obtained with the 1D-CNN model. The relative difference is given by $\Delta = ((M_{Q=2} - M_{Q=1})/M_{Q=1}) \times 100$ computed using the column means.

	$Q = 2$	$Q = 1$	$\Delta\%$
Validation AUC	0.829 ± 0.010	0.823 ± 0.004	+0.73
Validation AP	0.862 ± 0.010	0.856 ± 0.004	+0.70
Test AUC	0.831 ± 0.011	0.824 ± 0.003	+0.85
Test AP	0.863 ± 0.010	0.856 ± 0.003	+0.82
Validation TPR			
FAR 0.1	0.599 ± 0.023	0.580 ± 0.011	+3.28
FAR 0.01	0.422 ± 0.026	0.408 ± 0.014	+3.43
FAR 0.001	0.333 ± 0.033	0.326 ± 0.025	+2.15
Test TPR			
FAR 0.1	0.600 ± 0.028	0.585 ± 0.010	+2.56
FAR 0.01	0.424 ± 0.026	0.411 ± 0.012	+3.16
FAR 0.001	0.337 ± 0.032	0.331 ± 0.024	+1.81

4. Cross-Validation, Threshold Calibration, and Evaluation

To evaluate the performance of the 1D and 2D CNN classifiers described in Secs. II C 2 and II C 3, we reserve a stratified hold-out test set comprising 20% of the data, which is not used during training or threshold selection. This ensures that neither the model parameters nor the operating thresholds are influenced by the test data. The remaining data are used for stratified K -fold cross-validation with $K = 10$, reducing sensitivity to the choice of validation split. The networks are trained as binary classifiers by minimising the binary cross-entropy loss. Unless otherwise specified, optimisation is performed using the Adam optimiser with a learning rate of 5×10^{-4} and a batch size of 1000.

To mitigate overfitting and promote generalisation, early stopping is applied independently within each fold based on the validation AUC, with a patience of five epochs.

To characterise performance under both moderate and more constraining false alarm conditions, decision thresholds, τ , are determined on the validation set of each fold to achieve target false alarm rates (FARs) of 10^{-1} , 10^{-2} , and 10^{-3} , by calibrating τ against the distribution of negative samples. These calibrated thresholds are then applied to the held-out test set to measure the corresponding FAR and true positive rate (TPR), reflecting performance under fixed decision thresholds. In addition, threshold-independent metrics, including the area under the receiver operating characteristic curve (AUC) and the average precision (AP), are reported to quantify the overall discriminative performance of the classifiers, see Table III.

TABLE III. Comparison of results for different detection models. Performance is reflected by the threshold-agnostic metrics AUC (area under the ROC curve) and AP (average precision) on the test set, using the best fold. Finally, the TPR is given for a target FAR of 10%. Unless otherwise stated, $(J, Q) = (7, 2)$ is used.

Model	AUC	AP	TPR _{0.1}
Log Reg	0.815	0.847	0.562
1D-CNN			
$(J, Q) = (7, 2)$	0.844	0.876	0.636
$(J, Q) = (8, 2)$	0.832	0.863	0.597
$(J, Q) = (6, 2)$	0.845	0.876	0.622
2D CNN			
Log-scale	0.841	0.872	0.630
Raw	0.814	0.849	0.563
Large	0.826	0.858	0.580

III. NUMERICAL EXPERIMENTS AND RESULTS

In this section, we present numerical experiments to evaluate eccentricity detection performance using the WST representations of the simulated GW strain data described in Sec. II A, using different classification models, namely the 1D and 2D CNN architectures introduced in Secs. II C 2 and II C 3.

A. Detection Performance on Wavelet Scattering Representation

Across a range of experiments, we identify the 1D-CNN architecture applied to WST data using $(J, Q) = (7, 2)$ to be the best-performing configuration overall, and we adopt it as our reference model in the following—see also App. B. The confusion matrix for a target FAR of 10% and the ROC-curve are shown in Figs. 3 and 4, respectively.

Detailed metrics are shown in Table II, alongside results for $(J, Q) = (7, 1)$ to illustrate the benefit of increasing the scattering depth, Q , which corresponds to incorporating additional frequency-dependent structure. While decreasing the scale J or increasing Q further can yield modest additional improvements, the dimensionality of the WST representation grows rapidly, see App. C. As a result, $(J, Q) = (7, 2)$ represents an optimal trade-off between performance and feature dimensionality. Increasing J from 7 to 8 instead reduces classification accuracy, likely due to a bigger temporal averaging that suppresses informative structure. Table III provides a top-level comparison of the classifiers, demonstrating that the 1D-CNN consistently outperforms logistic regression, Sec. II C 1.

Using the default 2D-CNN configuration, the best-performing fold achieves a test AUC of 0.841 after 24 epochs. The corresponding TPRs are 63.0% at target FARs of 10%, respectively.

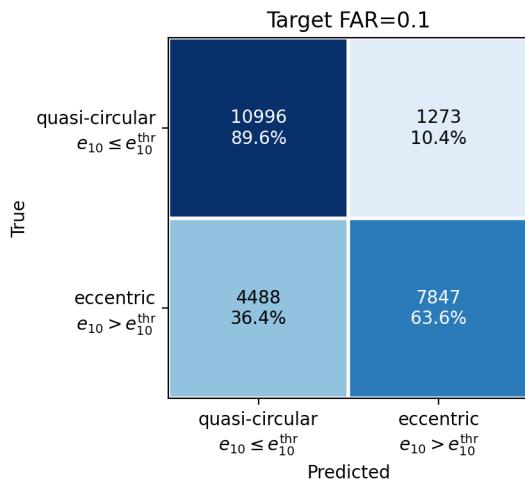


FIG. 3. Confusion matrix obtained for the reference 1D-CNN model and $J = 7, Q = 2$ WST coefficients, tuned to a target FAR of 10% on the validation set.

As shown in Table III, omitting the logarithmic rescaling (*Raw*) of the WST coefficients degrades performance, confirming the importance of dynamic-range compression for effective feature extraction. Increasing the model complexity to approximately twice the number of trainable parameters does not improve performance, as reflected by the results for the *Large* model in Table III, indicating that the baseline architecture is already sufficient to capture the relevant structure in the data.

Overall, the 2D-CNN achieves performance comparable to the 1D-CNN with a similar number of trainable parameters, but requires substantially longer training times. We train the LR and 1D-CNN on a MacBook Pro (M3 chip): the LR requires ~ 12 minutes, including hyperparameter optimization, and the 1D-CNN typically requires ~ 10 minutes for 10-fold cross-validation. The 2D-CNN is computationally more demanding and is trained on the CSD3 cluster (Ampere nodes) in Cambridge, UK, using one A100 GPU and 32 CPU cores, resulting in significantly greater computational overhead for comparable predictive performance.

The similar performance of the 1D and 2D CNN architectures indicates that preserving the two-dimensional structure of the WST coefficients does not provide a significant advantage. In contrast to conventional time–frequency representations such as Q-transforms, WST coefficients do not require explicit image-based interpretation. Instead, their informative content can be effectively captured using one-dimensional representations, enabling simpler models to achieve comparable performance with substantially lower computational cost.

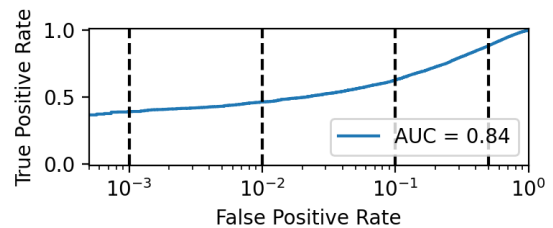


FIG. 4. ROC curve and AUC on the test set, for the best fold during training of the 1D-CNN model with $J = 7, Q = 2$ WST coefficients.

B. Weakly Eccentric Systems, Network SNR and False Negatives Distribution

We expect weakly eccentric systems, i.e. binaries with eccentricities close to the class threshold $e_{10}^{\text{thr}} = 0.01$, to be more difficult to distinguish from quasi-circular systems, and therefore more likely to be misclassified. To verify this, we focus on eccentric binaries in the test set ($e_{10} > e_{10}^{\text{thr}}$). Given our uniform sampling prior, the eccentricity distribution in this subset is expected to be approximately uniform, as confirmed in Fig. 5. We then extract the subset classified as circular by the reference 1D-CNN classifier, i.e. the false negatives (FNs), using a decision threshold calibrated to a target FAR of 10%. The eccentricity distribution of this FN subset is skewed toward lower values of e_{10} , consistent with the expectation that weakly eccentric systems are more difficult to distinguish from circular ones. This result indicates that the classifier identifies highly eccentric binaries with greater confidence, while misclassifications are concentrated near the class boundary.

The strength of a GW signal depends primarily on the binary masses and luminosity distance, which have a dominant impact on the signal-to-noise ratio (SNR). To investigate which of these physical parameters affect classifier performance, we examine the dependence on total mass M , mass ratio $q = m_2/m_1 < 1$, and NSNR. We define subsets of the test set corresponding to lower mass ratio ($q < 0.6$), lower total mass ($M < 50 M_{\odot}$), and lower NSNR (< 30), and compute the FN fraction within each subset. The FN fraction as a function of eccentricity is shown in Fig. 5. We find that the mass ratio has little impact on classifier performance, while total mass has a moderate effect. In contrast, the NSNR is the dominant factor, with lower-SNR events exhibiting significantly higher FN rates. The dependence of the FN fraction on these parameters is shown explicitly in Fig. 8.

C. Contribution of Higher Multipoles

To quantify the impact of higher multipoles on eccentricity detection, we train the 1D-CNN classifier using SEOBNRv5EHM waveforms restricted to the dominant quadrupole mode, $(\ell, m) = (2, 2)$, and evaluate perfor-

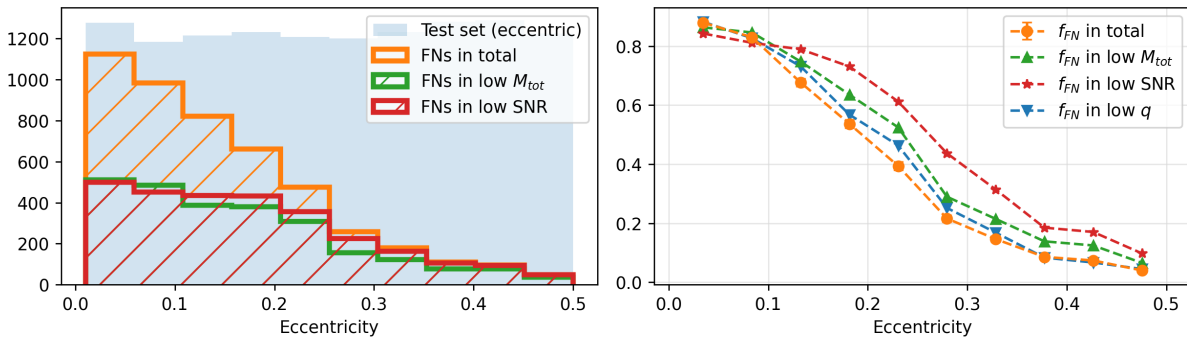


FIG. 5. (left) Histogram of eccentricity values for eccentric samples (i.e. those with $e_{10} > 0.01$) in both the test set and the set of false negatives (FNs), for the reference 1D-CNN with threshold tuned to a FAR of 10%. Additionally, histograms are also shown for the FN in the subset of binaries with lower $M_{tot} < 50M_{\odot}$, and the subset with lower NSNR < 30 . (right) Fraction of FN as a function of the bins on in the left panel. Fractions are calculated within the subsets of lower M_{tot} , NSNR or mass ratio q (where lower q corresponds to $q < 0.6$).

mance on data that include all multipoles. The results are summarized in Table IV. Training on the quadrupole-only WST representation yields robust classification performance, with test AUC ≈ 0.83 and stable detection efficiency across all operating points considered. This demonstrates that the quadrupole mode captures the dominant eccentricity-dependent structure present in the scattering coefficients.

The quadrupole-only and all-modes models exhibit statistically consistent performance across all metrics. The full model achieves marginally lower test AUC and AP, with relative difference of 0.36% and 0.23%, respectively. However, we find these differences small compared to the fold-to-fold variation and do not indicate a statistically significant improvement. Detection efficiencies at fixed false-alarm rates are similarly consistent between the two models. On the validation set, the quadrupole-only model yields slightly higher TPR at all FAR thresholds, while on the independent, full model, test set the two models agree to within $\lesssim 1.45\%$ across all operating points.

The ability of the 1D-CNN to achieve strong performance using only quadrupole information reflects its capacity to extract nonlinear temporal features from the scattering coefficients. At the same time, the lack of improvement obtained by including higher multipoles suggests that their contribution to eccentricity detection is subdominant in the mass range considered here, 10–40 M_{\odot} . Higher multipoles are expected to play a more important role for systems with larger mass ratios or stronger mode asymmetries.

D. Binaries with Spin-Induced Precession

Eccentricity and spin-induced precession can produce qualitatively similar amplitude and phase modulations in GW signals [e.g., 14]. Hence, classifiers trained to

TABLE IV. Performance comparison for quadrupole-only vs. full (all-modes) model using the 1D-CNN. Results are reported over $K = 10$ folds. Values are mean and standard deviation across folds. The relative difference is defined as $\Delta = [(M_{quad} - M_{all})/M_{all}] \times 100$, computed using the column means.

	Quadrupole	All modes	$\Delta(\%)$
Validation AUC	0.831 ± 0.015	0.829 ± 0.010	+0.24
Validation AP	0.864 ± 0.014	0.862 ± 0.010	+0.23
Test AUC	0.828 ± 0.013	0.831 ± 0.011	-0.36
Test AP	0.861 ± 0.012	0.863 ± 0.010	-0.23
Validation TPR			
FAR 0.1	0.61 ± 0.03	0.60 ± 0.02	+1.67
FAR 0.01	0.43 ± 0.04	0.42 ± 0.03	+2.38
FAR 0.001	0.34 ± 0.04	0.33 ± 0.03	+3.03
Test TPR			
FAR 0.1	0.60 ± 0.03	0.60 ± 0.03	+0.00
FAR 0.01	0.43 ± 0.04	0.42 ± 0.03	+2.38
FAR 0.001	0.34 ± 0.04	0.34 ± 0.03	+0.00

identify eccentricity may instead respond to precession-induced features. To assess this potential degeneracy, we apply our classifier to a test set of quasi-circular, precessing BBHs generated using the SEOBNRv5PHM approximant [56], which belongs to the same waveform family as the eccentric SEOBNRv5EHM model used during training, ensuring consistency in waveform modelling. We adopt standard BBH priors defined in Bilby, with the reference frequency for spin definitions fixed at 10 Hz.

The degree of spin-precession is quantified using the effective precession parameter χ_p [56],

$$\chi_p = \frac{1}{B_1 m_1^2} \max\left(B_1 m_1^2 \chi_{1,\perp}, B_2 m_2^2 \chi_{2,\perp}\right), \quad (16)$$

where $m_1 \geq m_2$ are the component masses, $B_i = 2 + 3m_{\neq i}/m_i$, and $\chi_{i,\perp}$ is the component of the dimensionless spin perpendicular to the orbital angular momentum. To ensure broad coverage of the

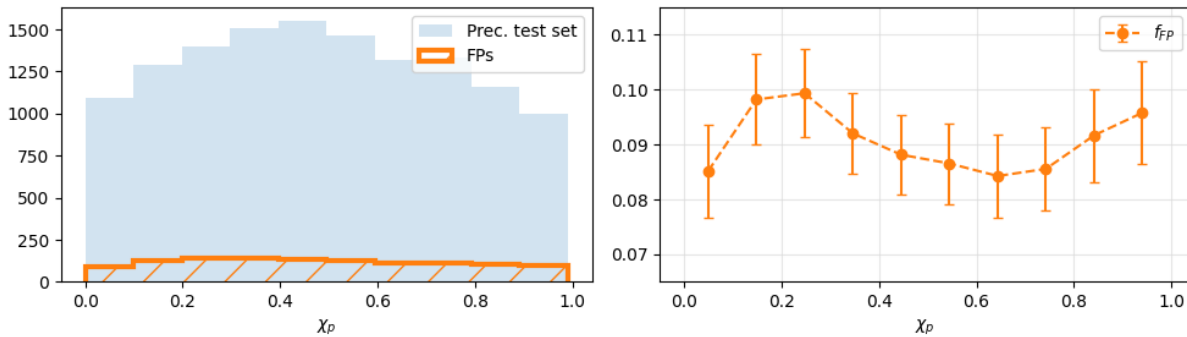


FIG. 6. (left) Histogram of χ_p values in the precessing circular binary dataset, as well as the subset classified as false positives (FPs) by the reference 1D-CNN model, tuned to a FAR of 10%. (right) Fraction of FPs in the different bins in the left panel.

precession parameter space, we draw spin magnitudes from β -distributions with parameters $\alpha = \beta = 0.5$, which preferentially sample both small and near-extremal spin values, thereby enhancing coverage in χ_p .

To understand how precession affects the scattering representation, we examine the first-order scattering coefficients, S_1 , defined in Eq. (4), for precessing waveforms described by Eq. (D7). The wavelet transform of $h(t)$ at scale $\lambda = (j, q)$ is given by:

$$W[h](\lambda, t) = \int_{-\infty}^{\infty} h(v) \cdot \psi_{\lambda}(t - v) dv. \quad (17)$$

The first-order scattering coefficients are obtained by taking the modulus of the wavelet transform and subsequently averaging over time. Using the wavelet expression Eq. (2), the first-order coefficients satisfy the bound

$$S_1(\lambda, t) \leq C \int dt \int dv \left| \sum_{m'} d_{mm'}^{\ell}(\beta) A_{\ell m'}(t) e^{-\frac{(t-v)^2}{2\sigma^2}} \right|, \quad (18)$$

where C is a constant. Since this expression explicitly shows that the mode-mixing coefficients $d_{mm'}^{\ell}(\beta)$, which arise from spin-induced precession, directly modify the scattering coefficients relative to the non-precessing case. This term does not appear in the **SEOBNRv5EHM** model, thus leading to different WST representations, see App. D.

Figure 6 shows the fraction of precessing binaries misclassified as eccentric by the reference 1D-CNN classifier, calibrated to a FAR of 10%. Across all values of χ_p , the FP fraction remains $\lesssim 10\%$, consistent with the targeted FAR. Importantly, this fraction does not increase significantly with increasing χ_p , even though these regions of the parameter space are *not* represented in the training data. This demonstrates that the classifier does not strongly confuse precession-induced waveform modulations with eccentricity signatures. Instead, its false positive rate remains consistent with the calibrated operating point, indicating that the WST-based representation

captures features that distinguish eccentricity from spin-induced precession [57]. It should be noted that these conclusions may change when the classifier is applied to data that is generated by an approximant that includes both eccentricity and spin-induced precession effects.

IV. DISCUSSION AND CONCLUSIONS

1. Definition of Eccentricity

Eccentricity decreases during the inspiral due to gravitational radiation reaction to GWs, and its observational signatures are therefore expected to be more prominent at earlier times. Lower-mass binaries remain in the detector band for longer durations prior to merger, and one might expect eccentricity to be easier to detect in such systems.

However, our results initially suggest the opposite, with classifier performance appearing to improve for higher-mass binaries (Fig. 7). This behaviour is explained by a correlation between total mass and NSNR in our dataset, as higher-mass binaries tend to produce stronger signals, partly due to the restricted luminosity distance range. To disentangle these effects, we examine the FN fraction as a function of total mass while restricting to lower-SNR events ($\text{NSNR} < 30$), thus reducing this correlation. Under this restriction, higher-mass binaries become more difficult to classify correctly, as shown in Fig. 7. This is consistent with expectations, since higher-mass binaries have shorter observable inspirals, reducing the visibility of eccentricity signatures.

The unexpected results for the performance as function of total mass may be further exacerbated by the definition of eccentricity used to label the dataset, namely the eccentricity evaluated at a fixed reference frequency of 10 Hz. We only capture the last 8 s of the signal in the WST, which, for lower-mass binaries, omits much of the frequency content in the longer inspiral. This reduces the SNR in the portion of the signal we analyse, and means that we study a less eccentric part of the signal, since

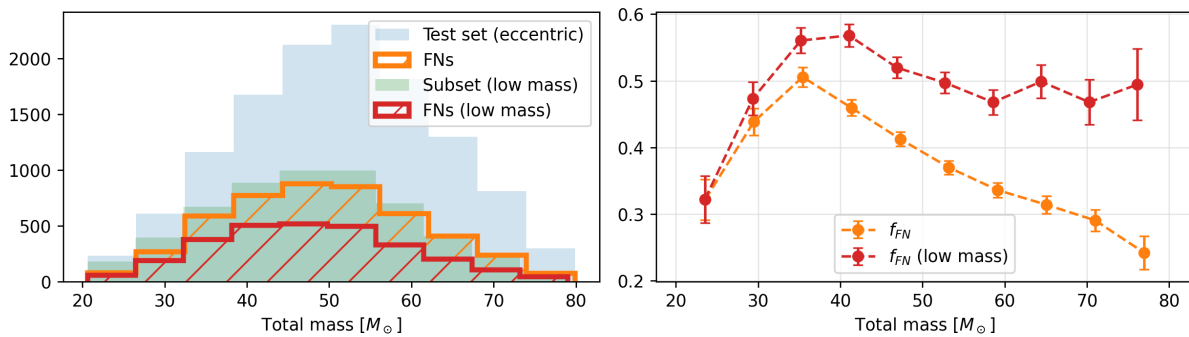


FIG. 7. (left) Histogram showing the distribution of total mass within the set of eccentric binaries, and within the subset with low (< 30) NSNR. The hatched histograms reflect the false negatives (FNs) in both of these sets. (right) Fraction of FNs within the set of eccentric binaries, and within the subset with low (< 30) NSNR, for the bins in the left panel.

eccentricity decreases with frequency as a result of GW emission [6]. As a result, binaries labeled as eccentric at 10 Hz may appear nearly circular over the part of the signal that we pass to the classifier, increasing the likelihood of misclassification.

2. Conclusions and Future Work

In this work, we have demonstrated that the WST provides a robust and physically meaningful representation for identifying orbital eccentricity in gravitational-wave signals embedded in realistic detector noise. We show that the WST encodes eccentricity-dependent structure in a deformation-stable and multiscale representation, enabling effective discrimination between eccentric and quasi-circular binaries. Using this representation, we have evaluated three classifier architectures—logistic regression, a one-dimensional CNN, and a two-dimensional CNN—and found that the one-dimensional CNN achieves strong detection performance while maintaining computational efficiency, indicating that the essential eccentricity information is already captured in the wavelet scattering coefficients.

From the physical factors that can influence classification performance, we found that signal-to-noise ratio is the dominant driver of detection efficiency, while total mass and mass ratio play secondary roles once correlations with signal strength are controlled.

Additionally, we showed that we can achieve strong performance using only quadrupole information, indicating that the dominant eccentricity signatures are captured by nonlinear features in the scattering coefficients. The lack of improvement from higher multipoles suggests that their contribution is subdominant for the mass range 10–40 M_{\odot} , though they are expected to become more important for systems with larger mass ratios or stronger mode asymmetries.

We also investigate whether our classifiers confuse signatures of spin-induced precession with those of eccen-

tricity, and apply them on a test set of quasi-circular waveforms generated with SEOBNRv5PHM [58], a state-of-the-art model that allows for misaligned spins. We find that our classifiers have consistent performance across the whole range of χ_p , which quantifies the degree of precession. This suggests that the WST may be a very informative representation to distinguish eccentric binaries from precessing ones.

This work can be extended and improved in different directions. On the one hand, the proposed framework can be extended to perform joint detection and parameter estimation, and explore higher mass range. On the other hand, we could use alternative eccentricity definitions—to better align with the observable signal—and assess performance on broader regions of parameter space.

V. ACKNOWLEDGMENTS

The authors thank Adhrit Ravichandran and Dr Rudy Morel for their helpful comments, and especially Dr Christopher Moore for his valuable insights. We are also grateful to Prof. Carola-Bibiane Schönlieb for her support, and to the Bristol Supercomputing Centre for computational resources. Additional computations were done on the CSD3 cluster (Cambridge).

P. C. M. is supported by a Daphne Jackson Fellowship sponsored by the Alan Turing Institute. S. J. S. is supported by the Centre for Doctoral Training at the University of Cambridge, funded by STFC. I. M. R-S acknowledges support from the STFC Ernest Rutherford Fellowship, grant number UKRI2423.

VI. APPENDIX

Appendix A: The 1D wavelet Scattering Transform

Following the notation used in KYMATIO [51], the scattering transform is defined relative to the duration of the

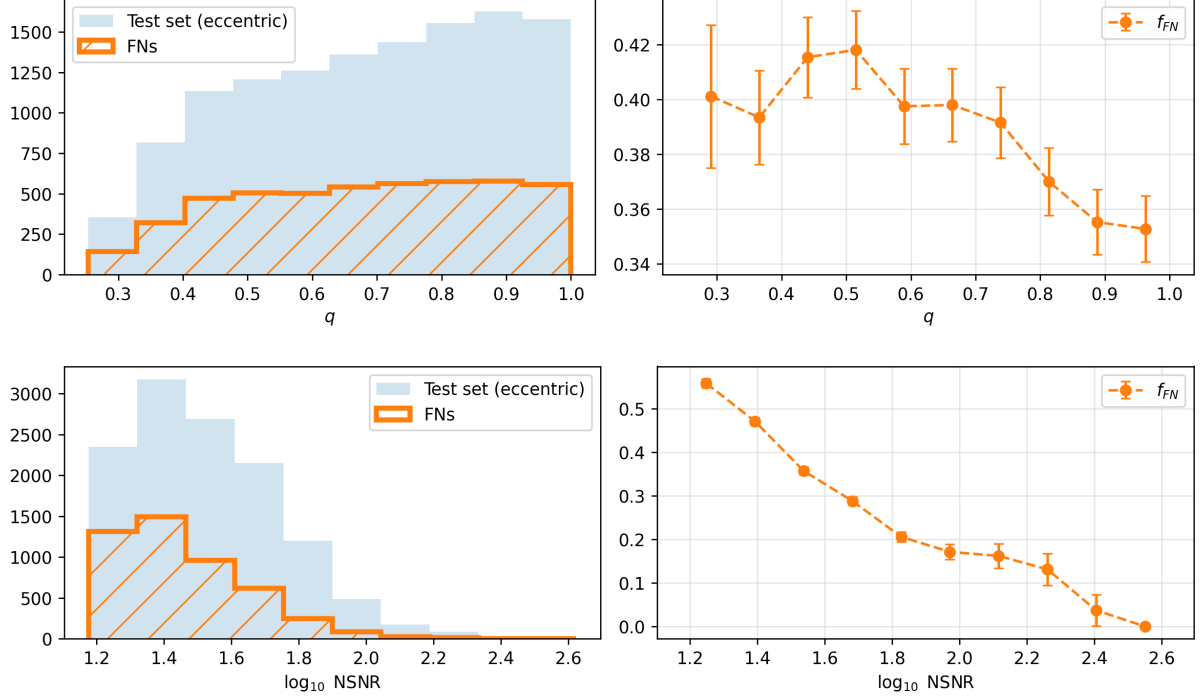


FIG. 8. (*left*) Histograms showing the distribution of mass ratio q and NSNR in 1) the subset of eccentric binaries in the test set and in 2) the set of false negatives (FNs), i.e. those of set (1) that are incorrectly identified as quasi-circular. (*right*) Fraction of FNs in the eccentric part of the test set, i.e. the ratio of the histograms on the left.

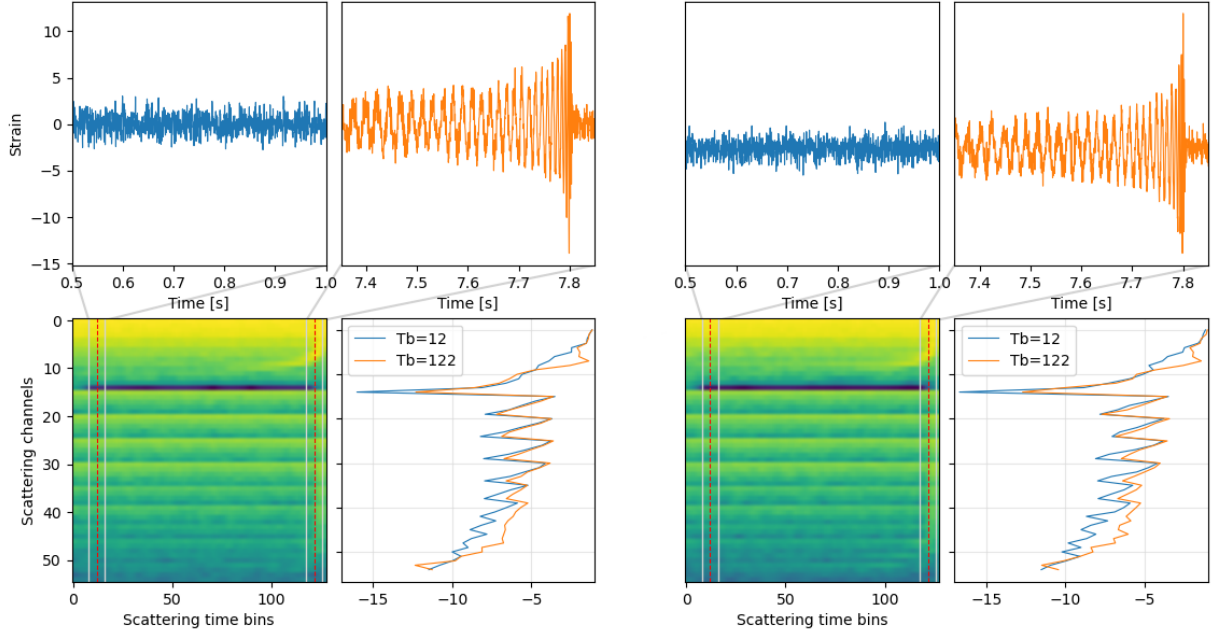


FIG. 9. Same as Fig. 1, but now after injecting the waveforms in Gaussian noise sampled from the LIGO Hanford detector PSD, and whitening the latter again.

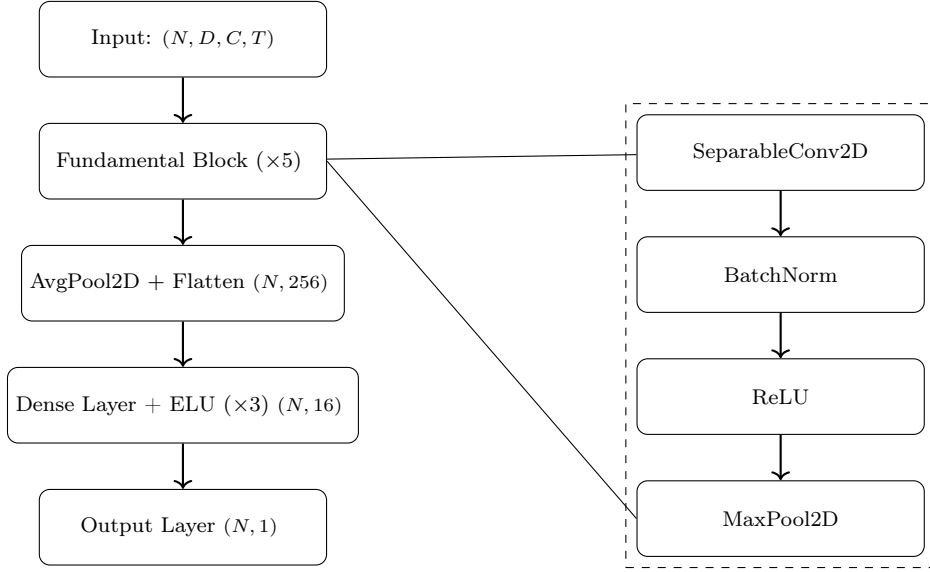


FIG. 10. Two-component diagram of SWT_CNN_2D. Left: high-level architecture showing the input, fundamental layer ($5 \times$ Fundamental Block), global pooling, dense layers, and output. Right: zoom-in of a Fundamental Block (SeparableConv2D + BatchNorm + ReLU + MaxPool). Tensor shapes are denoted as (N, D, C, T) .

input signal. In our case, the wavelet scattering transform (WST) is applied to a discretised detector strain signal $h(t)$ of duration T and sampling frequency f_s . The total number of time samples is therefore $N = Tf_s$. The fundamental frequency resolution of the signal is set by the base frequency

$$\nu_0 = \frac{1}{T}, \quad (\text{A1})$$

which defines the lowest resolvable frequency scale.

The scattering transform filter bank is composed of wavelets indexed by $\lambda = (j, q)$, where $j = 1, \dots, J$ labels the octave (dyadic scale), and $q = 0, \dots, Q - 1$ labels the position within each octave. The associated wavelet center frequencies are given by

$$f_{j,q} = \nu_0 2^{j-1+\frac{q}{Q}}, \quad (\text{A2})$$

which produces a logarithmic tiling of the frequency domain. The width parameter $\sigma_{j,q}$ determines the temporal width of the Gaussian. In `Kymatio`, the width parameter is chosen as

$$\sigma_{j,q}(f_{j,q}, Q) = \frac{1}{f_{j,q} (2^{1/Q} - 2^{-1/Q})}, \quad (\text{A3})$$

which ensures approximately constant relative bandwidth across scales.

The characteristic frequency associated with octave j is

$$\nu_j = 2^j \nu_0 = \frac{2^j}{T}, \quad (\text{A4})$$

up to a factor of order unity determined by the wavelet shape. This construction yields a constant- Q filter bank

covering the physically accessible frequency range

$$\nu_0 \lesssim f_{j,q} \lesssim \frac{f_s}{2}, \quad (\text{A5})$$

where the lower bound is set by the signal duration and the upper bound by the Nyquist frequency. Increasing the index j increases the wavelet center frequency, while increasing q improves frequency resolution within each octave.

In the time domain, each wavelet has a characteristic temporal support $\Delta t_{j,q}$ inversely proportional to its bandwidth,

$$\Delta t_{j,q} \sim \frac{1}{\Delta f_{j,q}} \sim \frac{Q}{f_{j,q}}, \quad (\text{A6})$$

so that high-frequency wavelets probe rapid oscillations, while low-frequency wavelets capture slower modulations of the signal [59].

Thus, the parameter Q controls the frequency resolution of the scattering transform. Larger values of Q provide finer frequency resolution within each octave, while smaller values improve temporal localization.

The averaging scale J determines the temporal support of the low-pass filter $\phi_J(t)$ and sets the largest temporal scale retained in the scattering representation. The corresponding temporal invariance scale is

$$\tau_J = \frac{2^J}{f_s}. \quad (\text{A7})$$

This parameter controls the trade-off between temporal resolution and invariance to time translations. In practice, J is chosen such that

$$\tau_J \lesssim T, \quad (\text{A8})$$

ensuring that the averaging window does not exceed the duration of the analyzed strain segment. In this work, detector data segments have duration $T = 8$ s. At a sampling frequency of 2048 Hz, choosing $J = 7$ thus sets $\tau_J = 1/16$ s.

Appendix B: Choosing the WST Resolution

The WST is parameterized by J and Q (see Sec. II B), which should be chosen based on the properties of the data, e.g. the duration of the signal and the sampling frequency. Our strain data has a fixed length of 8 seconds, and is sampled at 2048 Hz (giving a Nyquist frequency of 1024 Hz). We know that the LVK detectors become sensitive above ~ 10 Hz, which corresponds to the largest scale we want to resolve. Taking $J = 7$ (8) corresponds to an averaging scale of $1/16$ ($1/8$) seconds, which thus provides a good reference point. A good value of Q is a priori less obvious, and needs to balance a large frequency bank with sufficiently broad frequency bandwidths – see App. A.

In order to find the optimal J and Q , we performed a range of eccentricity detection experiments using the LR classifier and 1D and 2D CNNs II C. We found (see from Table III) that the best results are obtained for $(J, Q) = (7, 2)$ [60].

Appendix C: Dimensionality of the 1D Scattering Transform

In `Kymatio` the dimensionality of the scattering coefficients for an input signal of shape $x \in \mathbb{R}^{B \times T}$, where B denotes the batch size and T the temporal length of the signal, is [51]:

$$S_J(x) \in \mathbb{R}^{B \times C \times T_b}, \quad (\text{C1})$$

where

- C is the number of scattering coefficients (i.e. the number of admissible scattering paths),
- $T_b = T/2^J$ is the temporal resolution after averaging at scale 2^J .

The number of coefficients C depends on the maximum scattering order m_{\max} and on the parameters J and Q , where J controls the maximum scale and Q denotes the number of wavelets per octave.

For first-order scattering ($m_{\max} = 1$), the number of coefficients is approximately

$$C \approx 1 + JQ, \quad (\text{C2})$$

where the term 1 corresponds to the zeroth-order coefficient.

For second-order scattering, S_2 , one obtains approximately [31, 51]:

$$C \approx 1 + JQ + \frac{J(J-1)Q}{2}, \quad (\text{C3})$$

up to admissibility constraints that enforce scale ordering (e.g. $j_2 > j_1$).

Hence, the second order is quadratic in J .

$$C = \mathcal{O}(J^2Q). \quad (\text{C4})$$

Appendix D: SEOBNRv5EHM and SEOBNRv5PHM

A gravitational-wave waveform can be decomposed as [61, 62]

$$h(t; \iota, \varphi_0) = \frac{1}{D_L} \sum_{\ell, m} h_{\ell m}(t) {}_{-2}Y_{\ell m}(\iota, \varphi_0), \quad (\text{D1})$$

where D_L is the luminosity distance and (ι, φ_0) describe the source orientation.

In the effective-one-body (EOB) formalism, the $h_{\ell m}$ modes are constructed from the orbital dynamics [63–66]. `SEOBNRv5EHM` [27] and `SEOBNRv5PHM` [58] have the same EOB backbone dynamics but differ in their treatment of eccentricity and spin precession respectively.

`SEOBNRv5EHM` is designed to incorporate eccentricity effects, and in the circular limit its modes take a simple form [27, 65, 67]:

$$h_{\ell m}^{\text{EHM}}(t) = A_{\ell m}(t) e^{-i\phi_{\ell m}(t)}, \quad (\text{D2})$$

with phase

$$\phi_{\ell m}(t) = m\Phi_{\text{orb}}(t) + \delta_{\ell m}(t), \quad (\text{D3})$$

where $\Phi_{\text{orb}}(t)$ is the orbital phase and $\delta_{\ell m}(t)$ contains post-Newtonian and non-quasicircular corrections [68, 69]. Each mode is therefore governed by a single dynamical phase variable,

$$h_{\ell m}^{\text{EHM}}(t) = A_{\ell m}(t) e^{-i[m\Phi_{\text{orb}}(t) + \delta_{\ell m}(t)]}. \quad (\text{D4})$$

On the other hand, `SEOBNRv5PHM` incorporates precession by constructing the waveform in a co-precessing frame and rotating to the inertial frame [58, 66]:

$$h_{\ell m}^{\text{PHM}}(t) = \sum_{m'} D_{mm'}^{\ell}(\alpha, \beta, \gamma) h_{\ell m'}^{\text{copr}}(t), \quad (\text{D5})$$

where $D_{mm'}^{\ell}$ are Wigner rotation matrices parameterized by the time-dependent Euler angles (α, β, γ) [70]. The effective spin precession, χ_p , Eq. 16 measures the magnitude of the spin components perpendicular to the instantaneous orbital angular momentum $\hat{\mathbf{L}}(t)$ that drive precession, and therefore sets the time scale of the dependence of the Euler angles (α, β, γ) appearing in Eq. (D5),

which in turn control the strength of mode mixing and the resulting amplitude and phase modulations in the inertial-frame waveform modes [56, 66, 71, 72].

The co-precessing modes retain the aligned-spin struc-

$$h_{\ell m}^{\text{PHM}}(t) = \sum_{m'} D_{mm'}^{\ell}(\beta) A_{\ell m'}^{\text{copr}}(t) e^{-i[m\alpha + m'\gamma + m'\Phi_{\text{copr}} + \delta_{\ell m'}]}. \quad (\text{D7})$$

We can see that while SEOBNRv5EHM contains independent modes characterized by a single orbital phase, the

ture,

$$h_{\ell m}^{\text{copr}}(t) = A_{\ell m}^{\text{copr}}(t) e^{-i[m\Phi_{\text{copr}}(t) + \delta_{\ell m}(t)]}. \quad (\text{D6})$$

Substituting yields the inertial-frame modes,

precession effects in the SEOBNRv5PHM modes contain additional phases (α, γ) and mixing controlled by β that produce additional amplitude and phase modulations.

-
- [1] The LIGO Scientific Collaboration *et al.*, “GWTC-4.0: Updating the Gravitational-Wave Transient Catalog with Observations from the First Part of the Fourth LIGO-Virgo-KAGRA Observing Run,” *arXiv e-prints*, p. arXiv:2508.18082, Aug. 2025.
- [2] The LIGO Scientific Collaboration *et al.*, “GWTC-4.0: Population Properties of Merging Compact Binaries,” *arXiv e-prints*, p. arXiv:2508.18083, Aug. 2025.
- [3] J. Stegmann, F. Antonini, A. Olejak, S. Biscoveanu, V. Raymond, S. Rinaldi, and B. Flanagan, “In-plane Black-hole Spin Measurements Suggest Most Gravitational-wave Mergers Form in Triples,” *arXiv e-prints*, p. arXiv:2512.15873, Dec. 2025.
- [4] F. Antonini, I. Romero-Shaw, T. Callister, F. Dosopoulou, D. Chattopadhyay, M. Gieles, and M. Mapelli, “Gravitational waves reveal the pair-instability mass gap and constrain nuclear burning in massive stars,” *arXiv e-prints*, p. arXiv:2509.04637, Sept. 2025.
- [5] H. Tong, T. A. Callister, M. Fishbach, E. Thrane, F. Antonini, S. Stevenson, I. M. Romero-Shaw, and F. Dosopoulou, “A subpopulation of low-mass, spinning black holes: signatures of dynamical assembly,” *arXiv e-prints*, p. arXiv:2511.05316, Nov. 2025.
- [6] P. C. Peters, “Gravitational radiation and the motion of two point masses,” *Physical Review*, vol. 136, pp. B1224–B1232, nov 1964.
- [7] F. Antonini, S. Toonen, and A. S. Hamers, “Binary Black Hole Mergers from Field Triples: Properties, Rates, and the Impact of Stellar Evolution,” *Astrophys. J.*, vol. 841, p. 77, June 2017.
- [8] J. Samsing, “Eccentric black hole mergers forming in globular clusters,” *Phys. Rev. D*, vol. 97, p. 103014, May 2018.
- [9] I. Romero-Shaw, P. D. Lasky, and E. Thrane, “Four Eccentric Mergers Increase the Evidence that LIGO-Virgo-KAGRA’s Binary Black Holes Form Dynamically,” *Astrophys. J.*, vol. 940, p. 171, Dec. 2022.
- [10] N. Gupte, A. Ramos-Buades, A. Buonanno, J. Gair, M. C. Miller, M. Dax, S. R. Green, M. Pürrer, J. Wildberger, J. Macke, I. M. Romero-Shaw, and B. Schölkopf, “Evidence for eccentricity in the population of binary black holes observed by LIGO-Virgo-KAGRA,” *arXiv e-prints*, p. arXiv:2404.14286, Apr. 2024.
- [11] M. d. L. Planas, A. Ramos-Buades, C. García-Quirós, H. Estellés, S. Husa, and M. Haney, “Reanalysis of binary black hole gravitational wave events for orbital eccentricity signatures,” *Phys. Rev. D*, vol. 112, p. 123004, Dec. 2025.
- [12] G. Morras, G. Pratten, and P. Schmidt, “Orbital eccentricity in a neutron star - black hole binary,” *arXiv e-prints*, p. arXiv:2503.15393, Mar. 2025.
- [13] Y. Xu, J. Valencia, H. Estellés Estrella, A. Ramos Buades, S. Husa, M. Rosselló-Sastre, J. Llobera Querol, F. Ramis Vidal, M. de Lluc Planas Llompart, M. Colleoni, E. Hamilton, A. Montava Agudo, J. Yévana Carrilero, and A. Heffernan, “Parameter estimation for the GWTC-4.0 catalog with phenomenological waveform models that include orbital eccentricity and an updated description of spin precession,” *arXiv e-prints*, p. arXiv:2512.19513, Dec. 2025.
- [14] I. M. Romero-Shaw, D. Gerosa, and N. Loutrel, “Eccentricity or spin precession? distinguishing subdominant effects in gravitational-wave data,” *Monthly Notices of the Royal Astronomical Society*, vol. 519, pp. 5352–5357, jan 2023.
- [15] K. Divyajyoti, Sumit, S. Tibrewal, I. M. Romero-Shaw, and C. K. Mishra, “Blind spots and biases: The dangers of ignoring eccentricity in gravitational-wave signals from binary black holes,” *Phys. Rev. D*, vol. 109, p. 043037, Feb. 2024.
- [16] Divyajyoti, I. M. Romero-Shaw, V. Prasad, K. Paul, C. Kant Mishra, P. Kumar, A. Maurya, M. Boyle, L. E. Kidder, H. P. Pfeiffer, and M. A. Scheel, “Biased parameter inference of eccentric, spin-precessing binary black holes,” *arXiv e-prints*, p. arXiv:2510.04332, Oct. 2025.
- [17] S. Tibrewal, A. Zimmerman, J. Lange, and D. Shoemaker, “Misinterpreting Spin Precession as Orbital Eccentricity in Gravitational-Wave Signals,” *arXiv e-prints*, p. arXiv:2601.02260, Jan. 2026.
- [18] E. Payne, S. Hourihane, J. Golomb, R. Udall, D. Davis, and K. Chatziioannou, “Curious case of GW200129: Interplay between spin-precession inference and data-quality issues,” *Phys. Rev. D*, vol. 106, p. 104017, Nov. 2022.
- [19] I. Romero-Shaw, J. Stegmann, H. Tagawa,

- D. Gerosa, J. Samsing, N. Gupte, and S. R. Green, “GW200208_222617 as an eccentric black-hole binary merger: Properties and astrophysical implications,” *Phys. Rev. D*, vol. 112, p. 063052, Sept. 2025.
- [20] M. Zevin, I. M. Romero-Shaw, K. Kremer, E. Thrane, and P. D. Lasky, “Implications of Eccentric Observations on Binary Black Hole Formation Channels,” *The Astrophysical Journal Letters*, vol. 921, p. L43, Nov. 2021.
- [21] D. A. Brown and P. J. Zimmerman, “Effect of eccentricity on searches for gravitational waves from coalescing compact binaries in ground-based detectors,” *Phys. Rev. D*, vol. 81, p. 024007, Jan. 2010.
- [22] B. Gadre, K. Soni, S. Tiwari, A. Ramos-Buades, M. Haney, and S. Mitra, “Detectability of eccentric binary black holes with matched filtering and unmodeled pipelines during the third observing run of LIGO-Virgo-KAGRA,” *Phys. Rev. D*, vol. 110, p. 044013, Aug. 2024.
- [23] A. Ramos-Buades, S. Tiwari, M. Haney, and S. Husa, “Impact of eccentricity on the gravitational-wave searches for binary black holes: High mass case,” *Phys. Rev. D*, vol. 102, p. 043005, Aug. 2020.
- [24] I. Romero-Shaw, J. Stegmann, G. Morras, A. Dorozsmai, and M. Zevin, “Astrophysical Implications of Eccentricity in Gravitational Waves from Neutron Star-Black Hole Binaries,” *arXiv e-prints*, p. arXiv:2512.16289, Dec. 2025.
- [25] I. M. Romero-Shaw, P. D. Lasky, and E. Thrane, “Searching for eccentricity: signatures of dynamical formation in the first gravitational-wave transient catalogue of LIGO and Virgo,” *Monthly Notices of the Royal Astronomical Society*, vol. 490, pp. 5210–5216, Dec. 2019.
- [26] G. Morras, G. Pratten, and P. Schmidt, “Improved post-Newtonian waveform model for inspiralling precessing-eccentric compact binaries,” *Phys. Rev. D*, vol. 111, p. 084052, Apr. 2025.
- [27] A. Gamboa *et al.*, “Seobnrν5ehm: Effective-one-body waveform model for eccentric, spin-aligned binary black holes with higher-order modes,” *arXiv e-prints*, p. arXiv:2412.12823, 2024.
- [28] S. Albanesi, R. Gamba, S. Bernuzzi, J. Fontbuté, A. Gonzalez, and A. Nagar, “Effective-one-body modeling for generic compact binaries with arbitrary orbits,” *Phys. Rev. D*, vol. 112, p. L121503, Dec. 2025.
- [29] A. Ravichandran, A. Vijaykumar, S. J. Kapadia, and P. Kumar, “Rapid identification and classification of eccentric gravitational wave inspirals with machine learning,” 2024.
- [30] E. Khalouei, C. G. Sabiu, H. M. Lee, and A. Gopakumar, “External attention transformer: A robust ai model for identifying initial eccentricity signatures in binary black hole events in simulated advanced ligo data,” *Journal of Cosmology and Astroparticle Physics*, vol. 2025, p. 028, oct 2025.
- [31] S. Mallat, “Group invariant scattering,” 2012.
- [32] J. Bruna and S. Mallat, “Invariant scattering convolution networks,” 2012.
- [33] A. Licciardi, D. Carbone, L. Rondoni, and A. Nagar, “Wavelet scattering transform for gravitational wave analysis: An application to glitch characterization,” *Phys. Rev. D*, vol. 111, p. 084044, Apr. 2025.
- [34] S. Cheng and B. Ménard, “How to quantify fields or textures? a guide to the scattering transform,” 2021.
- [35] S. Cheng, Y.-S. Ting, B. Ménard, and J. Bruna, “A new approach to observational cosmology using the scattering transform,” *Monthly Notices of the Royal Astronomical Society*, vol. 499, p. 5902–5914, Oct. 2020.
- [36] G. Valogiannis and C. Dvorkin, “Towards an optimal estimation of cosmological parameters with the wavelet scattering transform,” *Physical Review D*, vol. 105, May 2022.
- [37] G. Valogiannis, F. Villaescusa-Navarro, and M. Baldi, “Towards unveiling the large-scale nature of gravity with the wavelet scattering transform,” *Journal of Cosmology and Astroparticle Physics*, vol. 2024, p. 061, Nov. 2024.
- [38] H. Shimabukuro, Y. Xu, and Y. Shao, “Analyzing the 21-cm forest with wavelet scattering transform: Insight into non-gaussian features of the 21-cm forest,” *Physical Review D*, vol. 112, Sept. 2025.
- [39] R. Morel, G. Rochette, R. Leonarduzzi, J.-P. Bouchaud, and S. Mallat, “Scale dependencies and self-similar models with wavelet scattering spectra,” 2023.
- [40] R. Morel, S. Mallat, and J.-P. Bouchaud, “Path shadowing monte-carlo,” 2023.
- [41] S. Cheng, R. Morel, E. Allys, B. Ménard, and S. Mallat, “Scattering spectra models for physics,” *PNAS Nexus*, vol. 3, p. pgae103, mar 2024.
- [42] T. Angles and S. Mallat, “Generative networks as inverse problems with scattering transforms,” 2018.
- [43] A. Siahkoohi, R. Morel, M. V. de Hoop, E. Allys, G. Sainton, and T. Kawamura, “Unearthing insights into mars: Unsupervised source separation with limited data,” 2023.
- [44] G. Ashton, M. Hübner, P. D. Lasky, C. Talbot, K. Ackley, S. Biscoveanu, Q. Chu, A. Divakarla, P. J. Easter, B. Goncharov, F. Hernandez Vivanco, J. Harms, M. E. Lower, G. D. Meadors, D. Melchor, E. Payne, M. D. Pitkin, J. Powell, N. Sarin, R. J. E. Smith, and E. Thrane, “BILBY: A User-friendly Bayesian Inference Library for Gravitational-wave Astronomy,” *Astrophys. J. Supp. S.*, vol. 241, p. 27, Apr. 2019.
- [45] I. M. Romero-Shaw *et al.*, “Bayesian inference for compact binary coalescences with BILBY: validation and application to the first LIGO-Virgo gravitational-wave transient catalogue,” *Mon. Not. R. Astron. Soc.*, vol. 499, pp. 3295–3319, Dec. 2020.
- [46] A. Gamboa, A. Buonanno, R. Enficiaud, M. Khalil, A. Ramos-Buades, L. Pompili, H. Estellés, M. Boyle, L. E. Kidder, H. P. Pfeiffer, H. R. Rüter, and M. A. Scheel, “Accurate waveforms for eccentric, aligned-spin binary black holes: The multipolar effective-one-body model seobnrν5ehm,” *Physical Review D*, vol. 112, p. 044038, aug 2025.
- [47] A. Vijaykumar, A. G. Hanselman, and M. Zevin, “Consistent eccentricities for gravitational-wave astronomy: Resolving discrepancies between astrophysical simulations and waveform models,” *The Astrophysical Journal*, vol. 969, p. 132, jul 2024.
- [48] M. A. Shaikh, V. Varma, H. P. Pfeiffer, A. Ramos-Buades, and M. van de Meent, “Defining eccentricity for gravitational wave astronomy,” *Physical Review D*, vol. 108, p. 104007, nov 2023.
- [49] These correspond to $(\ell, m) = (2, 2), (2, 1), (3, 2), (3, 3), (4, 3), (4, 4)$.
- [50] The WST provides a time-frequency representation that extracts geometric invariants from signals while remaining stable under small deformations, including time warping. The coefficients are Lipschitz-continuous with respect to signal deformations, implying that waveforms differing by small time or frequency shifts yield similar scattering representations.
- [51] M. Andreux, T. Angles, G. Exarchakis, R. Leonarduzzi,

- G. Rochette, L. Thiry, J. Zarka, S. Mallat, J. Andén, E. Belilovsky, J. Bruna, V. Lostanlen, M. Chaudhary, M. J. Hirn, E. Oyallon, S. Zhang, C. Cella, and M. Eickenberg, “Kymatio: Scattering transforms in python,” 2022.
- [52] B. G. Patterson, S. M. Tomson, and S. Fairhurst, “Identifying eccentricity in binary black hole mergers using a harmonic decomposition of the gravitational waveform,” 2024.
- [53] T. Islam, G. Khanna, and S. E. Field, “Adding higher-order spherical harmonics in non-spinning eccentric binary black hole merger waveform models,” 2024.
- [54] The raw WST coefficients span several orders of magnitude, which can adversely affect neural network training.
- [55] A. Paszke, S. Gross, F. Massa, A. Lerer, J. Bradbury, G. Chanan, T. Killeen, Z. Lin, N. Gimelshein, L. Antiga, A. Desmaison, A. Köpf, E. Yang, Z. DeVito, M. Raison, A. Tejani, S. Chilamkurthy, B. Steiner, L. Fang, J. Bai, and S. Chintala, “Pytorch: An imperative style, high-performance deep learning library,” 2019.
- [56] A. Ramos-Buades, A. Buonanno, H. Estellés, M. Khalil, D. P. Mihaylov, S. Ossokine, L. Pompili, and M. Shiferaw, “Seobnr5p5m: Next generation of accurate and efficient multipolar precessing-spin effective-one-body waveforms for binary black holes,” 2023.
- [57] We have repeated the analysis for a target FAR of 1%, and find again that the fraction of false positives in the precessing binaries dataset remains consistent with the target FAR.
- [58] L. Pompili *et al.*, “Seobnr5p5m: A next-generation effective-one-body model for precessing binary black holes with higher harmonics,” *arXiv e-prints*, p. arXiv:2303.18046, 2023.
- [59] J. Andén, V. Lostanlen, and S. Mallat, “Joint time-frequency scattering for audio classification,” in *2015 IEEE 25th International Workshop on Machine Learning for Signal Processing (MLSP)*, pp. 1–6, IEEE, sep 2015.
- [60] Other setups involved $J \in \{6, 7, 8\}$, $Q \in \{1, 2, 4\}$.
- [61] K. S. Thorne, “Multipole expansions of gravitational radiation,” *Reviews of Modern Physics*, vol. 52, no. 2, pp. 299–339, 1980.
- [62] L. E. Kidder, “Using full information when computing modes of post-newtonian waveforms from inspiralling compact binaries in circular orbit,” *Physical Review D*, vol. 77, no. 4, p. 044016, 2008.
- [63] A. Buonanno and T. Damour, “Effective one-body approach to general relativistic two-body dynamics,” *Physical Review D*, vol. 59, no. 8, p. 084006, 1999.
- [64] T. Damour, P. Jaranowski, and G. Schäfer, “On the determination of the last stable orbit for circular general relativistic binaries at the third post-newtonian approximation,” *Physical Review D*, vol. 62, no. 8, p. 084011, 2000.
- [65] Y. Pan, A. Buonanno, M. Boyle, L. T. Buchman, L. E. Kidder, H. P. Pfeiffer, and M. A. Scheel, “Inspirational-merger-ringdown waveforms of spinning, precessing black-hole binaries in the effective-one-body formalism,” *Physical Review D*, vol. 84, no. 12, p. 124052, 2011.
- [66] S. Ossokine *et al.*, “Multipolar effective-one-body waveforms for precessing binary black holes: Construction and validation,” *Physical Review D*, vol. 102, no. 4, p. 044055, 2020.
- [67] T. Damour, B. R. Iyer, and A. Nagar, “Improved resummation of post-newtonian multipolar waveforms from circularized compact binaries,” *Physical Review D*, vol. 79, Mar. 2009.
- [68] T. Hinderer and S. Babak, “Foundations of an effective-one-body model for coalescing binaries on eccentric orbits,” *Physical Review D*, vol. 96, Nov. 2017.
- [69] D. Chiaramello and A. Nagar, “Faithful analytical effective-one-body waveform model for spin-aligned, moderately eccentric, coalescing black hole binaries,” *Physical Review D*, vol. 101, May 2020.
- [70] S. Babak, A. Taracchini, and A. Buonanno, “Validating the effective-one-body model of spinning, precessing binary black holes against numerical relativity,” *Physical Review D*, vol. 95, Jan. 2017.
- [71] P. Schmidt, F. Ohme, and M. Hannam, “Towards models of gravitational waveforms from generic binaries: A simple approximate mapping between precessing and non-precessing inspiral signals,” *Physical Review D*, vol. 91, no. 2, p. 024043, 2015.
- [72] M. Hannam, P. Schmidt, A. Bohé, L. Haegel, S. Husa, F. Ohme, G. Pratten, and M. Pürrer, “Simple model of complete precessing black-hole-binary gravitational waveforms,” *Physical Review Letters*, vol. 113, p. 151101, 2014.